Research in Astronomy and Astrophysics, 23:035008 (10pp), 2023 March https://doi.org/10.1088/1674-4527/acb87a


# Probing the Variation of Reverberation Lags along with X-Ray Flux in the AGN Mrk 704

K. Sriram[1,2], Deblina Lahiri[1], Vivek K. Agrawal[3], D. Nour[1,4], and C. S. Choi[2]
[1] Department of Astronomy, Osmania University, Hyderabad 500007, India; astrosriram@yahoo.co.in
[2] Korea Astronomy and Space Science Institute, Daejeon 34055, Republic of Korea
[3] Space Astronomy Group, ISITE Campus, U. R. Rao Satellite Centre, Outer Ring Road, Marathahalli, Bangalore 560037, India
[4] Department of Physics, Faculty of Science, Al Baath University, Homs, Syria
*Received 2022 October 31; revised 2022 December 19; accepted 2023 January 3; published 2023 February 28*

## Abstract

Understanding the variation of lags with respect to the X-ray flux is important to explore the geometry of the inner region of the accretion disk in AGNs. We performed frequency-lag, energy–lag and spectral studies for two sets of observations, in order to investigate the variations in lags with respect to X-ray flux in the AGN source Mrk 704 using the XMM-Newton observatory. We divided one of the light curves into two sections which were noticed to exhibit a flux variation. The frequency-lag spectra in different energy domains revealed that reverberation (soft) lags varied along with the flux. For the first time, we show that the blurred reflection model can consistently explain the soft excess observed in the X-ray spectra for this source. The fluxes of soft (i.e., reflection) and hard components were noted to vary by ∼18% and ∼9% respectively, across the sections. The soft lag amplitude was found to be larger at the high flux state than the amplitude at the low flux state. Most importantly, we found that both frequency-lag and energy–lag spectra do not display significant variation between two observational data sets despite a flux variation of 43%. This phenomenon cannot be explained by the reflection model because the soft lag amplitudes must be larger in the high flux state. The probable scenario is that, in the low flux state, the obscuring cloud delays the reflected soft photons which increases the soft lag amplitude.

*Key words:* galaxies: active – galaxies: nuclei – accretion – accretion disks

## 1. Introduction

Active galactic nuclei (AGNs) at the center of galaxies are considered to be the primary contributors to the complex spectral and temporal behavior of these regions throughout the electromagnetic radiation spectrum. A physical interpretation of the variabilities occurring on a timescale of hours to days helps in deciphering the various radiative and structural entities in the inner region of AGNs lying across a few parsecs. Most of the radiation energy emanates from the accretion disk and the associated relativistic effect due to the strong gravitational influence of the supermassive black holes (SMBHs) primarily affects the soft (0.3–2 keV) and hard X-rays (>2 keV). The primary structure in the inner region of the accretion disk is the corona which exhibits a power-law like X-ray spectral continuum, whose location and structure have been widely debated. This illuminates the inner region of the accretion disk producing the relativistic disk reflection component that arises in the form of soft excess (Fabian et al. 2009; Nardini et al. 2012; Reis et al. 2012) and a skewed broad iron emission line around 6.4 keV observed in most AGNs (e.g., MCG-6-30-15; Tanaka et al. 1995).

Though most of the information can be perceived from the spectral domain, a study in the time domain also plays a key role in exploring the dynamics and geometry of the inner region of the accretion disk. One of the primary tools is the study of time lags between different energy bands pertaining to the characteristics of variability arising from the physical structures like the corona, and the inner and outer regions of the Keplerian portion of the disk. Hard lags (hard X-ray photons are delayed with respect to the soft photons) have been detected in many AGNs (e.g., De Marco et al. 2013; Kara et al. 2016) and were used to confine the role of the fluctuation propagation model (Lyubarskii 1997) or the thermal Comptonization model (Dasgupta & Rao 2006; Sriram et al. 2009). In the propagation model, fluctuation arises in the outer region of the disk that propagates toward the SMBH on a viscous diffusion timescale. Later, this fluctuation gets modulated in the coronal region emitting hard X-rays that are delayed with respect to the soft X-rays arising from the initial fluctuations (e.g., Kotov et al. 2001; Arevalo & Uttley 2006). However, this model finds it difficult to explain the soft lags or reverberation lags exhibited by many AGNs. The reverberation lags are robustly confirmed in the source 1H 0707-495 (Fabian et al. 2009; Zoghbi et al. 2010) and these are caused by the illumination of the coronal emission in the inner region of the disk, which is seen as the reflection continuum in the X-ray spectra. The difference in the

light travel distance between the coronal and reflected emission is observed as the soft lags.

De Marco et al. (2013) reported that 15 out of 32 AGNs exhibit reverberation lags in the frequency range of $0.07–4 \times 10^{-3}$ Hz with a lag timescale $\tau = 10–600$ s. Moreover, these lags are correlated with the mass of the SMBH making them an important parameter to understand the inner region of the accretion disk. On a few occasions, low-frequency soft lags are observed to vary with the flux in some sources like NGC 4051 (Alston et al. 2013), MCG-6-30-15 (Kara et al. 2014) and NGC 1365 (Kara et al. 2015), and for more similar sources see Kara et al. (2016). In IRAS 13 224-3809, the lag amplitude was found to vary with flux, i.e., a larger amplitude of soft lag was connected to the higher flux state (Kara et al. 2013). Therefore, a flux-dependent time lag study may also provide pivotal information on the variation of the coronal structure or the reflection process in the disk.

Mrk 704 is a Seyfert 1.2 galaxy with a redshift of $z = 0.029234$ (Veron-Cetty & Veron 2010). Spectral analysis of the XMM-Newton data sets in 0.5–10 keV implies the presence of warm absorbers associated with the torus and orbiting clouds around the nucleus (Matt et al. 2011). An independent investigation of the same data with different models suggests the presence of two blackbody components, along with two outflow components having characteristics of both the warm absorbers and emitters (Laha et al. 2011). For this source, Kara et al. (2016) found a hard lag in a low frequency range, which is a typical characteristic often seen in other AGNs along with a reverberation lag at a high frequency range. The motivation of our study is to depict and constrain the changes in the frequency and energy lag spectra in Mrk 704 with respect to the X-ray flux variation using the XMM-Newton data and for the first time the spectra were explained using the reflection model.

## 2. Data Reduction and Analysis

Mrk 704 was observed by the XMM-Newton on two occasions at an interval of about three years. Matt et al. (2011) reported a flux difference of about 40% between the two observations. The first observation was performed on 2005 October 21 (ObsId. 1: 0300240101) with a total exposure time of 21.7 ks for which the EPIC-PN and MOS1 cameras were operating in small window mode whereas MOS2 was in full frame mode. The second observation was performed on 2008 November 2 (ObsId. 2: 0502091601) having a total exposure time of 98.2 ks where EPIC-PN and MOS cameras were in small window mode, using a thin filter. The respective data were reduced using the Science Analysis Software (SAS) version 19.1.0. There was no photon pile-up found when checked with the epatplot task provided in SAS. We only used the PN data for our analysis because of its higher signal-to-noise ratio as compared to MOS. For both the first and second observations, a circular region of radius 40″ was taken to extract the source and the background region (source-free region) adopting PATTERN $\leqslant 4$. Data from these regions are used for both timing and spectral analysis. For timing analysis, we obtained the source and background light curves using the evselect task and then corrected the light curve to obtain the background subtracted light curve using the epiclccorr task. The top panel of Figure 1 shows the light curves of ObsId. 2 in two energy bands, viz. 0.3–2 keV and 2–10 keV. We have divided the light curves into two Sections, Sections 1 and 2, where Section 1 is from 0 to 40 ks and Section 2 has the remaining portion of the light curve. The division was based on the variation in hardness ratio (HR) shown in Figure 1 (top panel) where HR is defined as 2–10 keV/0.3–2.0 keV. The bottom panel of Figure 1 displays ObsId. 1 light curves in the same energy bands along with its HR. For spectral analysis, we have generated the redistribution matrix file (RMF) using the SAS task rmfgen and the ancillary response file (ARF) using the task arfgen. We applied XSPEC v 12.12.0 (Arnaud 1996) for spectral analysis and all the reported errors are at the 90% confidence level or otherwise mentioned.

## 3. Frequency–Lag Spectra

We examined the frequency–lag spectra for the two sections of ObsId. 2 in order to investigate whether there exists any difference or association with the spectral flux. To calculate the frequency–lag spectrum we relied on the technique outlined by Nowak et al. (1999). We extracted the energy-dependent light curves with a bin time of 50 s and divided them into equal intervals. Each interval has 16 temporal bins (each bin with a length of 50 s) for each time interval (i.e., 800 s). This binning was chosen to look for lags in the frequency range of $\sim 1 \times 10^{-3}$–$9 \times 10^{-3}$ Hz as we need to compare both the observations and one of them (ObsId. 1) is relatively small in duration. Later, we computed the cross–spectrum by multiplying one Fourier transformed light curve with a complex conjugate of the other Fourier transformed light curve, where the calculated phase is the phase difference between the two light curves. Later, the cross-spectrum was averaged over intervals, and then the argument of average cross-spectrum divided by $2\pi f$ gives the frequency-dependent time lag, where $f$ is the midpoint of the frequency bin.

Matt et al. (2011) studied the two observation sets of Mrk 704 and reported the presence of warm absorbers which are needed to explain the large residuals in the soft X-ray domain i.e., $<2.0$ keV after fitting a power-law model to the spectra. They noted weaker absorption in the second observation ObsId. 2 when compared to the first one. Hence we obtained frequency–lag spectra as shown in Figure 2 for different energy bands (0.3–0.4 keV versus 0.6–0.8 keV, 2–4 keV and

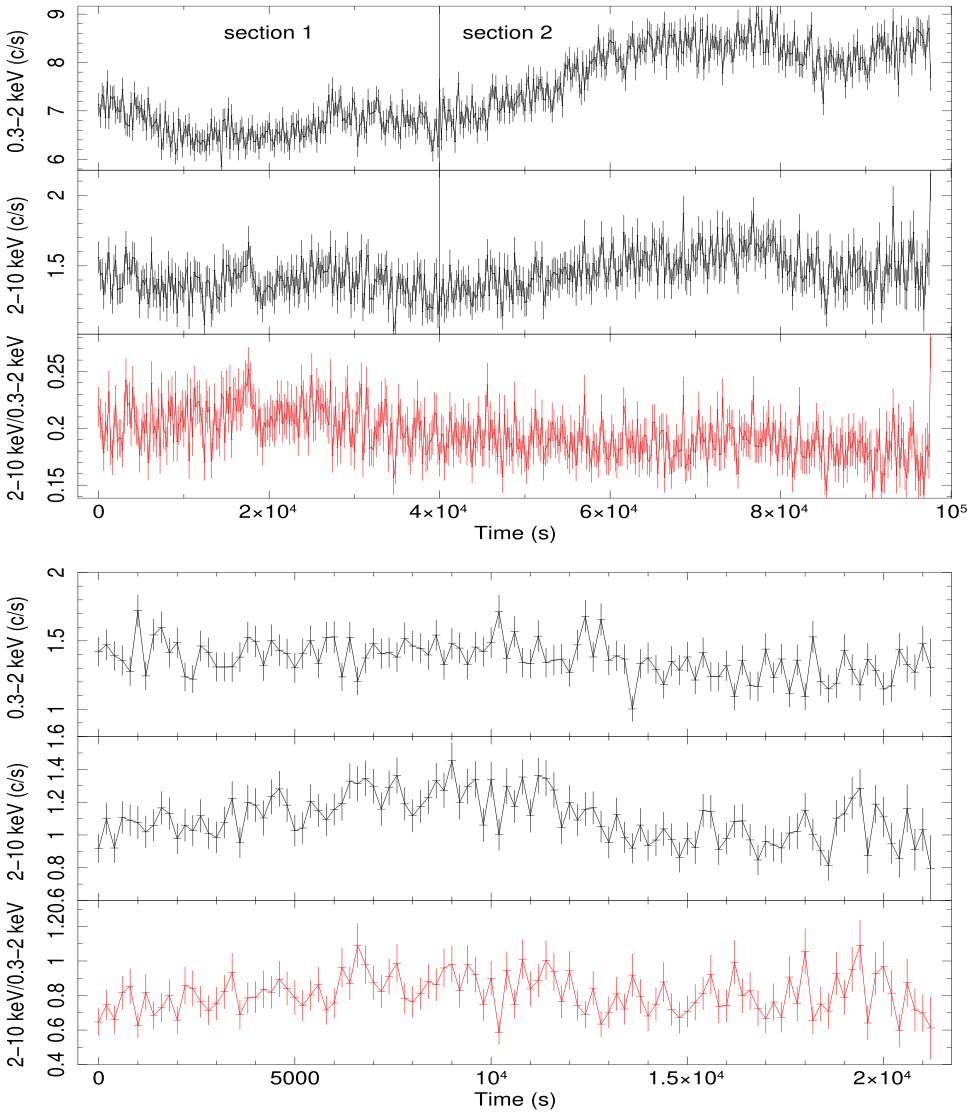


**Figure 1.** (Top) The 200 s binned light curve of ObsId. 2 in the different energy bands and the vertical line marks the division as Sections 1 and 2 along with HR. (Bottom) The 200 s binned light curve of ObsId. 1 in 0.3–10 keV.

4–10 keV) of Sections 1 and 2 of ObsId. 2 and ObsId. 1. Even though 0.3–0.4 keV has a narrow soft energy range, it results in a larger lag in the spectra. The star and triangle symbols are associated with Sections 1 and 2 of ObsId. 2 respectively, whereas circle symbols correspond to ObsId. 1. We noticed lag amplitude differences in Sections 1 and 2 below $4 \times 10^{-3}$ Hz for Sections 1 and 2 (within error bars) similar to the observation by Kara et al. 2013 for the AGN source IRAS 13224-3809. We also found that in different energy bands the source displays varying lag amplitudes (see Figure 2). In the case of ObsId. 1 (associated with low flux) the lags were closely displaying variations similar to those exhibited in Section 2 of ObsId. 2 associated with high flux. We also found that the lag trend reversed around $10^{-3}$ Hz (Figure 2 top and bottom panels). In order to understand the observed lags, we unfolded the spectra as discussed below. We also found that the lag trend reversed around $10^{-3}$ Hz (Figure 2 top and bottom panels). In order to understand the observed lags, we unfolded the spectra as discussed Section 5.

We obtained the frequency–lag spectra shown in Figure 3 between two different energy bands i.e., 0.3–2.0 keV and 2–10 keV. The choice of these bands is due to the fact that 0.3–2.0 keV is often considered to be due to the reflection component, i.e., hard X-ray photons are being reflected from the accretion disk resulting in the soft component. Whereas, 2–10 keV corresponds to hard X-rays associated with the

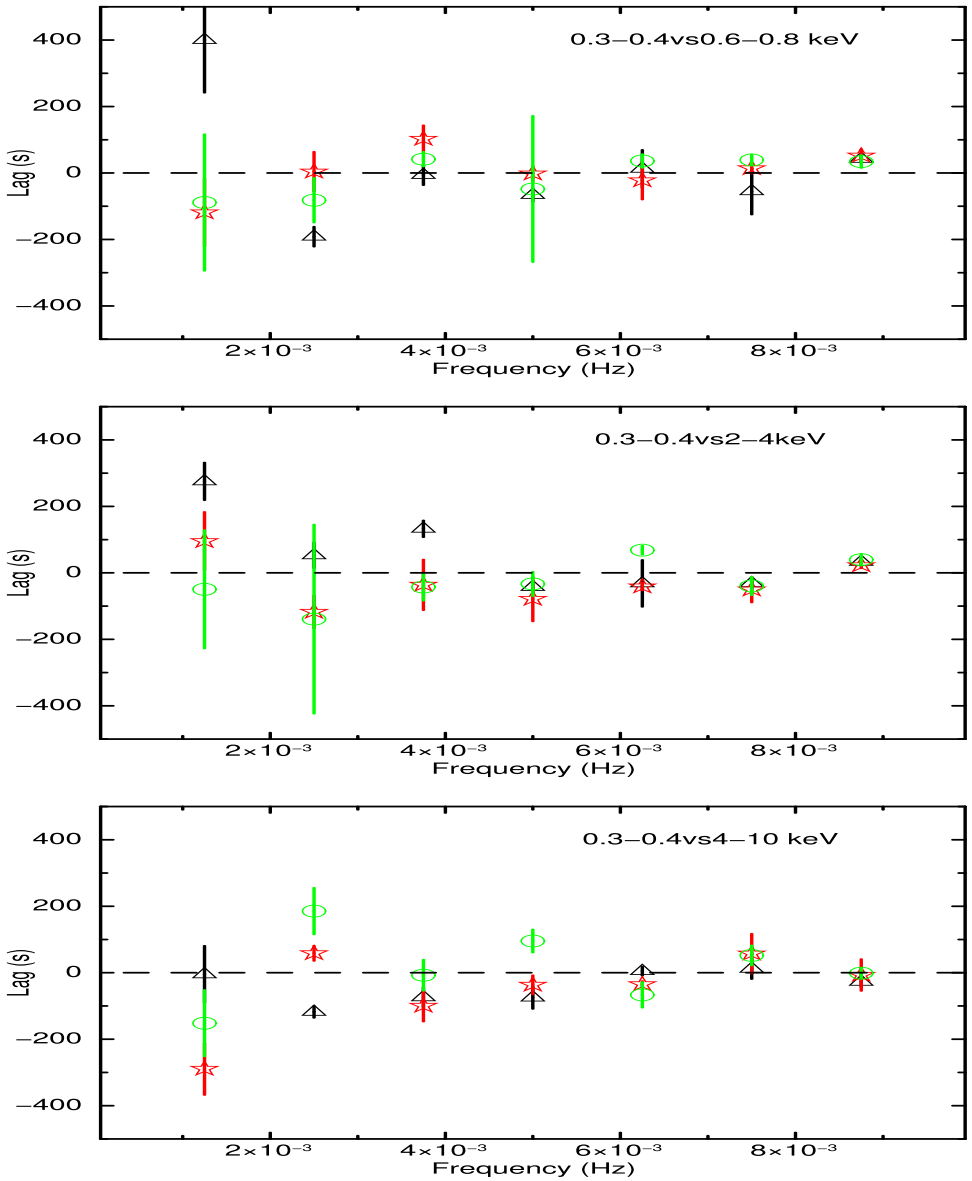


**Figure 2.** Frequency-lag spectra for different energy bands from top to bottom panels. The triangle and star symbols represent Sections 1 and 2 of the ObsId. 2 respectively, and the circle displays the same for ObsId. 1.

corona, i.e., the primary X-ray continuum. We perform the frequency–lag spectra for Sections 1 and 2 of ObsId. 2 and ObsId. 1.

We noticed the lag amplitude difference between Sections 1 and 2 is observed below 1–2 $\times$ $10^{-3}$ Hz within error bars and has also been noted at a higher frequency range on a few occasions. One of the most important features we observed is that again in ObsId. 1 (associated with low flux), the lag amplitudes were found to closely match with those of ObsId. 2 (high flux). In order to understand the observed lag variation, we unfolded the spectra as discussed below.

## 4. Energy–Lag Spectra

The lag variation of the reflection component with respect to flux can be inferred from the study of energy–lag spectra (e.g., Kara et al. 2013). For ObsId. 1 and sections of ObsId. 2, we obtained the energy–lag spectra at frequencies 1.1 $\times$ $10^{-3}$ Hz and 2.0 $\times$ $10^{-3}$ Hz. These frequencies were used because a

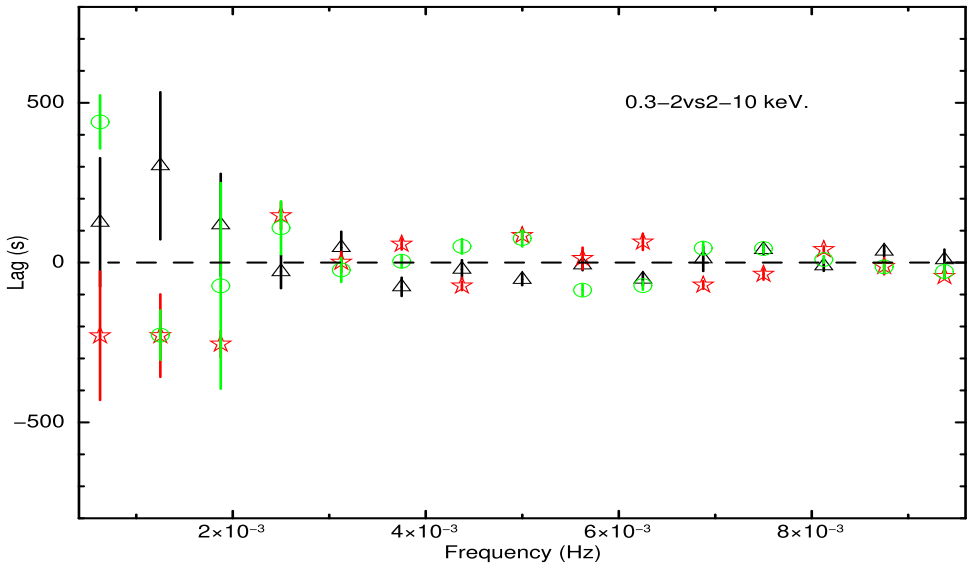


**Figure 3.** Frequency-lag spectra between the energy bands 0.3–2 and 2–10 keV. Symbols used have the same convention as described in Figure 2.

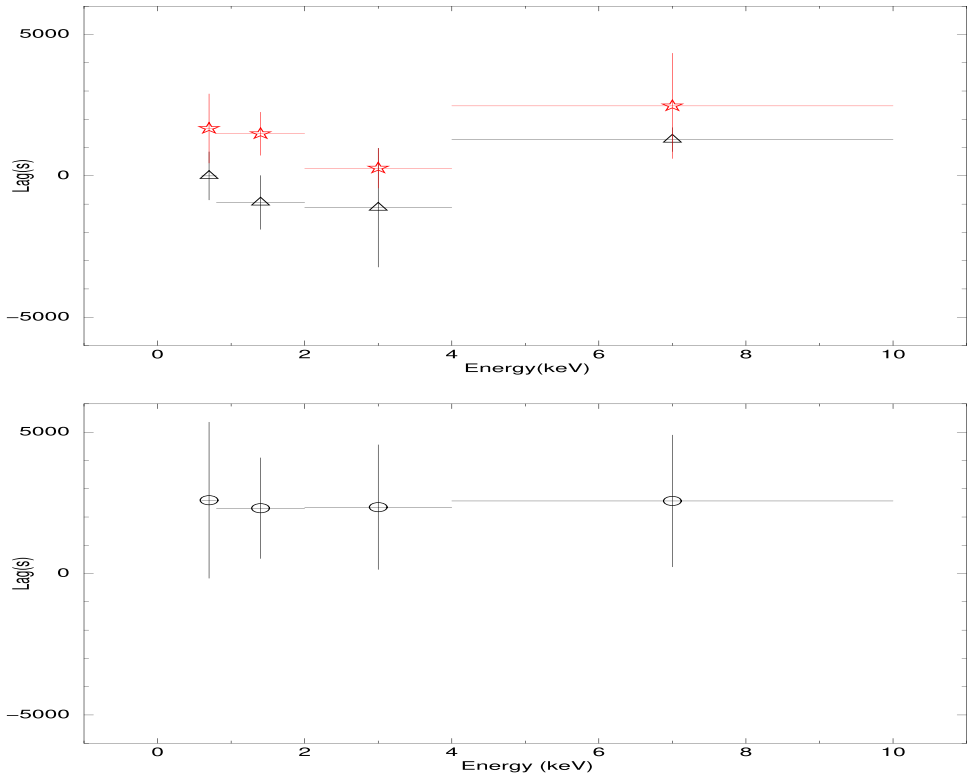


**Figure 4.** Energy-lag spectra at $1.1 \times 10^{-3}$ Hz: (top) the ObsId. 2, triangle and star symbols represent Sections 1 and 2 respectively. The vertical line marks the division of the two sections. (Bottom) The same for ObsId. 1.

minute variation within error bars in the frequency-lag spectra was noticed. We performed the cross-correlation function (CCF) analysis using the crosscor tool in XRONOS (Stella & Angelini 1992) between 0.3–0.6 keV and 0.6–0.8 keV, 0.8–2.0 keV, 2.0–4.0 keV and 4–10 keV (for more details see Brenneman et al. 2007; Sriram et al. 2009).

The peak of the CCF was fitted using a Gaussian function and error bars of lags are at 90% confidence level. Figure 4

displays the energy–lag spectra at $1.1 \times 10^{-3}$ Hz of sections (ObsId. 2) in top and ObsId. 1 in bottom panels. It can be seen that there is no relative variation in the energy–lag spectra between the observations. Also, no significant difference was observed between the energy–lag spectra connected to $1.1 \times 10^{-3}$ Hz and $2.0 \times 10^{-3}$ Hz. Kara et al. (2016) calculated the energy–lag spectrum at a low frequency $\sim 10^{-4}$ Hz in a different energy and did not compare it with the ObsId. 1 energy–lag spectrum. Kara et al. (2013) found that for higher reflection components, the soft lag amplitude is relatively high. However, we do not see such a variation in Mrk 704, even though a large flux variation exists between ObsId. 1 and 2.

## 5. Spectral Analysis

We analyzed the energy spectra in detail with the reflection model. In general, the X-ray spectra of AGNs in 0.3–10 keV can be modeled with a blurred reflection component along with other physical models (Fabian et al. 2009; Fabian et al. 2013; Kara et al. 2013). It has been shown that the soft excess exhibited by the AGN X-ray spectra can be well explained by the reflection model.

Initially, a simple power-law model did not result in a good fit ($\chi^2/\mathrm{dof} > 2$) and left large residuals in the lower energy range of 0.3–2 keV. Subsequently, we invoked the following model, zedge*TBabs (kdblur*(reflionx) + Gaussian + Power-law), to fit the spectra of ObsId. 1 and the two sections of ObsId. 2 (Figure 5). The Reflionx model consists of four parameters, viz. Fe abundance $Z_{\mathrm{Fe}}$ ($Z_{\odot}$), ionization parameter $\xi = 4\ \pi F_{\mathrm{tot}}/n_{\mathrm{H}}$ where $F_{\mathrm{tot}}$ is the illuminating flux and $n_{\mathrm{H}}$ is the density of the reflector, power-law index ($\Gamma$) which is the source of incident illumination, and redshift ($z = 0.0292$ for Mrk 704). The reflection component is blurred by the KDBLUR model which assumes a power-law emissivity index ($q$), an inner radius $r_{\mathrm{in}}$ and an outer radius ($r_{\mathrm{out}}$) in units of $r_g$ (gravitational radius) along with an inclination ($i$). First, we fixed the following parameters: $i = 40°$ (Matt et al. 2011), $r_{\mathrm{out}} = 400\ r_g$, $N_{\mathrm{H}} = 0.028 \times 10^{22}$ cm$^{-2}$ for the two sections of ObsId. 2 and $N_{\mathrm{H}} = 0.041 \times 10^{22}$ cm$^{-2}$ for ObsId. 1. Later, these parameters were freed when used with other models and fixed again when we determined the best-fit values. We fixed and tied the power-law index to the power-law index of the reflection model.

From the fit, the power-law index is determined to be $\Gamma = 1.85 \pm 0.12$ for Section 1 and $1.90 \pm 0.02$ for Section 2 (Table 1). The best-fit values for Section 1 are $q = 5.66 \pm 0.21$, $r_{\mathrm{in}} = 1.23 \pm 0.90\ r_g$, $Z_{\mathrm{Fe}} = 0.25 \pm 0.08$, $\xi = 198 \pm 27$ and Gaussian line centroid energy $(E_c) = 6.32 \pm 0.03$ keV. Similarly, the values for Section 2 are $q = 5.17 \pm 0.13$, $r_{\mathrm{in}} = 1.50 \pm 1.00\ r_g$, $Z_{\mathrm{Fe}} = 0.25 \pm 0.07$, $\xi = 199 \pm 30$ and $E_c = 6.34 \pm 0.04$ keV. Based on Table 1, there are no significant changes in the model parameters as the source varied from Sections 1 to 2. We calculated the total, reflected and power-law fluxes in 0.3–10 keV (Table 1). We noticed a variation of 18% in the reflection component of the spectra.

The spectral fit of the ObsId. 1 spectrum using the same model yields no significant variation in most of the model parameters when compared to that in ObsId. 2, except $\Gamma = 1.44 \pm 0.05$ (Table 1). The total flux in the 0.3–10 keV band is calculated to be $1.36 \times 10^{-11}$ erg cm$^{-2}$ s$^{-1}$. Matt et al. (2011) reported a flux variation of ∼39% in 0.5–10 keV band and we obtained a similar flux variation of 43% in total flux, 29% reflection flux, and more than 90% change in power-law flux between ObsId. 1 and 2 in 0.3–10 keV (see Table 1).

We also tried to fit the spectra by substituting zedge with the zxipcf model (see Matt et al. 2011). zxipcf is based on XSTAR photoionization code but with a limitation that the photon index is fixed at 2 for the ionizing continuum and elemental abundances are fixed to the solar abundances. This also gave a reasonable fit for Sections 1 and 2 with $\chi^2/\mathrm{dof} = 289/260$ and $368/358$, respectively (Table 2 and Figure 3). Here we fixed the inner radius $r_{\mathrm{in}}$ of the reflection model as $1.50\ r_g$. The soft and hard fluxes increased by 18% and 9% between Sections 1 and 2 of ObsId. 2 (Table 2). The ionization parameter $\log \xi$ has decreased in ObsId. 1 when compared with ObsId. 2 sections. It may be worthwhile to mention that the model fit resulted in a significant change in the absorption column density of the warm absorber from $N_{\mathrm{H}} = 5.16 \times 10^{22}$ cm$^{-2}$ (ObsId. 1) to $1.73 \times 10^{22}$ cm$^{-2}$ (Section 2 of ObsId. 2) together with a change in the power-law index.

## 6. Discussion

### 6.1. Lag Spectral Variation of ObsId. 2 Sections

We have studied the frequency and energy lag spectra and X-ray spectral properties of the AGN Mrk 704 for two different observations. In the present work, we noticed that the amplitudes of frequency lags were varying between the sections of ObsId. 2 at a few frequencies within error bars where the flux variation of the reflection component was about 18% (Table 1). In general, as the reflection component increases along with the flux, one should observe relatively more soft lags. This phenomenon was observed in the frequency-lag spectra where soft lags appeared during the high flux state (see Figure 2, triangle and star symbols). The difference in lag amplitudes is notable between the two sections, particularly in the range of 1–$4 \times 10^{-3}$ Hz of ObsId. 2 (Figure 2). We noted a lag amplitude difference of ∼200 s at $\sim 10^{-3}$ Hz and the difference decreases with increasing frequency (e.g., see top panel of Figure 2). In addition, the lag amplitude difference of ∼100 s is observed at $\sim 1 \times 10^{-3}$ Hz (bottom panel, Figure 2). In Figure 3, i.e., frequency lag spectra between 0.3–2.0 keV and 2–10 keV, it was observed that sections of ObsId. 2 display lag variations mostly $< 4 \times 10^{-3}$ Hz (e.g. a lag difference of 180 s was noted around $10^{-3}$ Hz), and smaller lag differences (<100 s) were observed

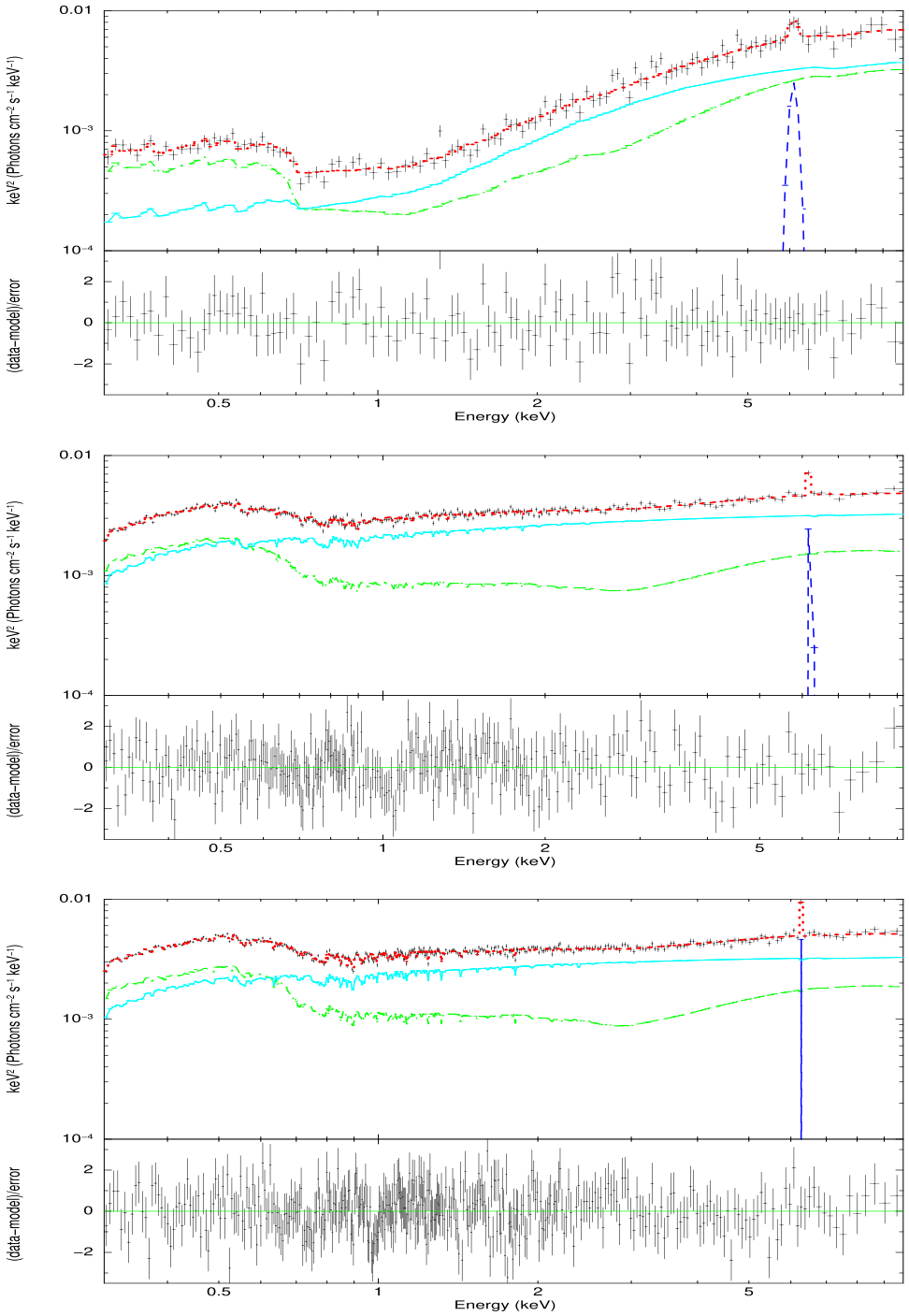


**Figure 5.** Unfolded spectra of ObsId. 1 followed by the spectra of Sections 1 and 2 of ObsId. 2. In the panels, the data are represented with a plus sign, the continuum with a dotted line (red), the reflection component with a dot–dashed line (green), the power-law component with a solid line (cyan) and the Gaussian line is represented with a dashed line (blue). The lower plot in each panel shows the $\Delta\ \chi^2$.

**Table 1**
Best-fit Results of the Spectra using the Model zedge*TBabs(kdblur*(reflionx) +Gaussian+Power-law)

| Parameters | ObsId. 2 (Section 1) | ObsId. 2 (Section 2) | ObsId.1 |
|---|---|---|---|
| $E_{edge}$(keV) | $0.74 \pm 0.01$ | $0.75 \pm 0.01$ | $0.39 \pm 0.01$ |
| $\tau_1$ | $0.19 \pm 0.01$ | $0.23 \pm 0.02$ | $0.93 \pm 0.09$ |
| $E_{edge}$(keV) | ... | ... | $0.70 \pm 0.02$ |
| $\tau_2$ | ... | ... | $0.69 \pm 0.10$ |
| $N_H(\times 10^{22})(cm^{-2})$ | 0.028 | 0.028 | 0.041 |
| Index($q$) | $5.66 \pm 0.21$ | $5.17 \pm 0.13$ | $6.91 \pm 0.31$ |
| $r_{in}(r_g)$ | $1.23 \pm 0.90$ | $1.50 \pm 1.00$ | $1.23 \pm 0.65$ |
| $r_{out}(r_g)$ | 400 | 400 | 400 |
| Inclination($i°$) | 40 | 40 | 40 |
| $Z_{Fe}(Z_\odot)$ | $0.25 \pm 0.08$ | $0.25 \pm 0.07$ | 0.99 |
| $\Gamma_1$ | $1.85 \pm 0.12$ | $1.90 \pm 0.02$ | $1.44 \pm 0.05$ |
| $\xi$(erg cm $s^{-1}$) | $198 \pm 27$ | $199 \pm 30$ | $113.73 \pm 16.10$ |
| $Norm_{ref}(\times 10^{-5})$ | $7.92 \pm 0.45$ | $6.34 \pm 0.69$ | $1.17 \pm 0.08$ |
| $E_{line}$(keV) | $6.32 \pm 0.03$ | $6.34 \pm 0.04$ | $6.20 \pm 0.06$ |
| $\sigma$(keV)$(\times 10^{-2})$ | $0.02 \pm 0.05$ | $0.10 \pm 0.07$ | $4.97 \pm 11.75$ |
| $Norm_g(\times 10^{-5})$ | 1.0 | 1.0 | 1.0 |
| $\Gamma_2$ | 1.85 | 1.90 | 1.44 |
| $Norm_{pl}(\times 10^{-3})$ | 2.41 | 2.67 | 0.10 |
| $\chi^2$/dof | 288/265 | 401/378 | 170/121 |
| $flux_T$(0.3–10 keV) | 2.26 | 2.54 | 1.36 |
| $flux_R$(0.3–10 keV) | 0.80 | 0.98 | 1.27 |
| $flux_{PL}$(0.3–10 keV) | 1.47 | 1.57 | 0.09 |

**Note.** The fluxes are in unit of $10^{-11}$ erg $cm^{-2}$ $s^{-1}$. All the uncertainties are at the 90% confidence level. The flux subscripts *T*, *R* and PL correspond to total, reflected and power-law components respectively.

**Table 2**
Best-fit Results of the Spectra Using the Model zxipcf*TBabs(kdblur*(reflionx) +Gaussian+power-law)

| Parameters | ObsId. 2 (Section 1) | ObsId. 2 (Section 2) | ObsId. 1 |
|---|---|---|---|
| $N_H(\times 10^{22})(cm^{-2})$ | $1.84 \pm 0.98$ | $1.73 \pm 0.74$ | $5.16 \pm 0.55$ |
| log$\xi$(zxipcf) | $2.06 \pm 0.13$ | $2.18 \pm 0.08$ | $0.80 \pm 0.23$ |
| $C_f$ | $0.35 \pm 0.07$ | $0.42 \pm 0.06$ | $0.88 \pm 0.01$ |
| $N_H^{TB}(\times 10^{22})(cm^{-2})$ | $0.033 \pm 0.004$ | $0.031 \pm 0.003$ | $0.031 \pm 0.010$ |
| Index (q) | $5.42 \pm 0.24$ | $4.87 \pm 0.14$ | $4.64 \pm 0.50$ |
| $r_{in}(r_g)$ | 1.50 | 1.50 | 1.50 |
| $r_{out}(r_g)$ | 400 | 400 | 400 |
| Inclination(i°) | 40 | 40 | 40 |
| $Z_{Fe}(Z_\odot)$ | $0.10 \pm 0.07$ | $0.10 \pm 0.05$ | $0.20 \pm 0.05$ |
| $\Gamma_1$ | 1.91 | 1.95 | 1.78 |
| $\xi$(erg cm $s^{-1}$) | $199.98 \pm 49.28$ | $198.12 \pm 47.34$ | $199.69 \pm 12.59$ |
| $Norm_{ref}$ $(\times 10^{-7})$ | $5.43 \pm 2.27$ | $6.19 \pm 2.74$ | $11.37 \pm 1.30$ |
| $E_{line}$(keV) | $6.31 \pm 0.03$ | $6.35 \pm 0.02$ | $6.27 \pm 0.10$ |
| $\sigma$(keV)$(\times 10^{-2})$ | 2.0 | 0.2 | 10.8 |
| $Norm_g(\times 10^{-5})$ | $1.08 \pm 0.28$ | $1.13 \pm 0.24$ | $2.14 \pm 1.26$ |
| $\Gamma_2$ | $1.91 \pm 0.03$ | $1.95 \pm 0.03$ | $1.78 \pm 0.02$ |
| $Norm_{pl}(\times 10^{-3})$ | $2.72 \pm 0.25$ | $2.96 \pm 0.51$ | $2.44 \pm 0.19$ |
| $\chi^2$/dof | 289/260 | 368/358 | 132/116 |
| $flux_T$(0.3–10 keV) | 2.30 | 2.59 | 1.37 |
| $flux_R$(0.3–10 keV) | 0.80 | 1.00 | 0.62 |
| $flux_{PL}$(0.3–10 keV) | 1.51 | 1.60 | 0.76 |

**Note.** The fluxes are in the unit of $10^{-11}$ erg $cm^{-2}$ $s^{-1}$. All the uncertainties are at the 90% confidence level. The flux subscripts *T*, *R* and PL correspond to total, reflected, and power-law components respectively.

at higher frequencies on a few occasions. The ObsId. 2 lag spectra variation closely matches that reported by Kara et al. (2016) but the lag amplitudes are different possibly due to different energy band selections. Moreover, we also show that there is not much difference in the energy–lag spectra between them (Figure 4). One of the most viable explanations for the results is that, in Section 2, the reflection has increased as deduced from the spectral analysis, causing relatively large amplitudes of soft lags. However, the coronal flux variation is relatively low compared to the reflected component. Similar relative variations were observed in the case of IRAS 13 224-3809 by Kara et al. (2013) at a frequency of $10^{-3}$ Hz.

Our study strongly suggests that the blurred reflection model can successfully explain the spectra and noticed that $\Gamma$ of the reflionx model has not varied significantly from Sections 1 to 2 of ObsId. 2 ($1.85 \pm 0.12$ and $1.90 \pm 0.02$) suggesting the presence of a strong and persistent corona (Table 1). It was also noticed that the ionization parameter remained the same, i.e., $\xi \sim 198$ (Table 2). The emissivity of the reflection model was parameterized by $\eta \propto r^{-q}$, where it decreases as we move away from the SMBH ($r^{-3}$), but significantly affects the emissivity near the SMBH due to a strong light-bending effect. Sometimes, the emissivity is steeper in the inner region of the accretion disk (Miniutti & Fabian 2004). We did not find any change in the emissivity index with $q \sim 5.20$ for Sections 1 and 2, indicating that the light bending in the inner region is strongly affecting the spectral continuum which is supported by the parameter $r_{in} = 1.23$–$1.50$ $r_g$. As the source varied from Sections 1 to 2, we observed that both soft and hard fluxes increased by ∼18% and ∼9% respectively (Table 2). Since the variation of soft lag was seen at a higher frequency around $1$–$4 \times 10^{-3}$ Hz, we conclude that the variation in soft X-ray flux is highly connected with the reflection component of the spectra.

In Section 1 of ObsId. 2, the X-ray flux was relatively low along with a low reflection component in comparison to those in Section 2. It was also noted that hard X-ray emission did not vary much across the sections. We, therefore, propose the following physical scenario where the Comptonization region or corona is relatively compact during Section 1 thus illuminating a smaller location of the inner region of the accretion disk, which also explains the smaller reverberation lags. In the case of Section 2, the corona was relatively sparse (less dense) and slightly extended which caused more reflection

flux to be emitted from the inner region of the disk. Alternatively, the higher reflection in Section 2 could also be due to an increase in the height of the corona above the inner region of the disk. Simultaneous observations by the XMM-Newton and NuSTAR satellites would be helpful in deciphering the role of the corona and the variable reflection component across different flux levels in Mrk 704 and their impact on the lags.

Here we use the regression relation to estimate the mass of SMBH in Mrk 704 evaluated by De Marco et al. (2013), viz. $\mathrm{Log}(\tau) = 1.98 \pm 0.08 + (0.59 \pm 0.11)\ \mathrm{Log}(M_7)$, where $\tau$ is the soft lag in units of s and $M_7$ is the mass of the SMBH in units of $10^7\ M_\odot$. The highest soft lag was around 254 s (at $2\times10^{-3}$ Hz) in the Section 2 frequency-lag spectrum where the obscuration is less (Figure 3). This mass was estimated to be $3.07–11.26 \times 10^7\ M_\odot$ and this range is well in agreement with the mass determined from the reverberation techniques, i.e., $8.2 \times 10^7\ M_\odot$ (Laha et al. 2011). Moreover, if we consider the error bars of the observed soft lag ($\pm$40 s), the result does not change.

### 6.2. Lag Spectral Variations between ObsId. 2 and ObsId. 1

Based on the spectral results, we noted 43% flux variation between ObsId. 1 and 2. Moreover, we noted a difference in the power-law index, i.e., $\Gamma = 1.44$ for ObsId. 1 and 1.87 for ObsId. 2 (Table 1) and the relative difference is also observed with another model (Table 2) well in agreement with the variations reported by Matt et al. (2011). The salient feature observed in the frequency-lag spectra of ObsId. 1 (low flux) is that it closely mimics the lag spectra of Section 2 of ObsId. 2 (high flux; see Figures 2 and 3). Moreover, we did not find any strong variation within error bars in the energy–lag spectra between ObsId. 1 and 2 (Figure 4). In general, the energy–lag amplitude increases along with an increase in the reflection flux (Kara et al. 2013).

Based on the variations in lag in Figures 2 and 3, we argue that since the ObsId. 1 is connected to a low flux state, it should exhibit low amplitude soft lags based on the reflection model (e.g., Kara et al. 2013) but the observed lags were comparable to the lags seen in the high flux state of ObsId. 2. It could be due to a physical scenario that during the ObsId. 1, the reflection component photons (soft photons) are traversing through the obscuring cloud which in turn increases the amplitude of the soft lags. Such clouds or warm absorbers are supported by previous spectral studies. The source variability is affected by the presence of a two-phased warm absorber having $\xi$ values of $10^{1.27}$ and $10^{2.7}$ with outflow velocities of 1350 km $s^{-1}$ and 450 km $s^{-1}$ (Laha et al. 2011) respectively. Matt et al. (2011) noticed similar physical properties that are responsible for the spectral variations in two of the observations. The column density, ionization parameters and covering fraction significantly varied between the two sets of observations which may be associated with the torus wind, partial covering scenario, or an accretion disk wind. The low ionization absorber was proposed based on the presence of clouds orbiting the vicinity of the nucleus. The effects of warm absorbers were studied in detail by Silva et al. (2016) who observed that their presence increases the lag amplitudes at different frequencies in NGC 4051. In the present work also, we found that the ionization parameter is significantly lower in ObsId. 1 ($\log \zeta = 0.80 \pm 0.23$) than a high ionization state seen in ObsId. 2 ($\sim\log \zeta = 2.12 \pm 0.11$). Such low ionization clouds shall cause the photons to lag further with respect to the primary one (Silva et al. 2016).

Future studies in the direction of lag amplitude variation along with X-ray flux are important because they will help us to understand the geometry of the accretion disk and corona, and demystify the presence of clouds (if any) in the outer region of the disk. Moreover, soft lags are often used to constrain the mass of an SMBH (e.g., De Marco et al. 2013), and hence any influence on the lags due to a flux variation will cause an overestimation of the SMBH mass.

## 7. Conclusion

Based on our results for the timing and spectral study of Mrk 704, we conclude the following:

1. The frequency-lag spectra in different energy bands of the two sections of ObsId. 2 exhibited lag amplitude differences at $\sim$1–4 $\times\ 10^{-3}$ Hz of the order of 100–300 s (Figures 2 and 3). The observed lag variation in frequency-lag spectra is consistent with the prediction of the reflection model that the soft lag amplitude should increase along with the high flux. Based on the observed soft lag, we estimated the mass of SMBH, $M = 3–11 \times 10^7\ M_\odot$.
2. No lag variations were observed between low and high flux state observations in energy–lag spectra. In the reflection model, a lag amplitude in energy–lag spectra is associated with a higher reflection flux. The absence of such variation indicates the presence of obscuring clouds in a low flux state.
3. In the case of ObsId. 1, the lags were well in agreement with the high flux state (Section 2) of ObsId. 2 despite a total flux variation of $\sim$43% and relatively harder $\Gamma$. The reflection model predicts that the amplitude of the soft lag should be low for a low flux state (Kara et al. 2013) but in the present study, it was found otherwise. Such lag amplitudes during a low flux state can be explained if clouds or warm absorbers were present which were responsible for delaying the photons seen in ObsId. 1. Due to this scenario the lags observed in both low and high flux states are similar to each other. Since Mrk 704 shows a flux variation of about 43% in the duration of 3

yr, it is quite possible that future observations will help us in understanding the lag variation with respect to the X-ray flux.

4. The soft excess in the X-ray spectrum of Mrk 704 can be explained using a blurred reflection model and during the observations, the inner disk radius was located at 1.35 $r_g$.

## Acknowledgments

We thank the referee for providing the suggestions which improved the quality of the paper. This work is based on observations obtained with XMM-Newton, an ESA science mission with instruments and contributions directly funded by ESA Member States and NASA. K.S. acknowledges the financial support from the Indian Space Research Organisation (ISRO), Government of India. V.K.A. thanks GH, SAG, DD, PDMSA and Director URSC for encouragement and continuous support to carry out this research. The contribution by C.S.C. is supported by the KASI project astrophysical research on gravity and radiation mechanism.

## Data Availability

Data used in this work can be accessed through the HEASARC website (https://heasarc.gsfc.nasa.gov/cgi-bin/W3Browse/w3browse.pl) and is also available with the authors.

## References

Alston, W. N., Vaughan, S., & Uttley, P. 2013, MNRAS, 429, 75
Arevalo, P., & Uttley, P. 2006, MNRAS, 367, 801
Arnaud, K. A. 1996, in ASP Conf. Ser. 105, Astronomical Data Analysis Software and Systems V, Vol. 101, ed. J. H. George & B. Jeannette (San Francisco, CA: ASP), 17
Brenneman, L. W., Reynolds, C. W., Wilms, J., & Kaiser, M. L. 2007, ApJ, 666, 817
Dasgupta, S., & Rao, A. R. 2006, ApJL, 651, 13
De Marco, B., Ponti, G., Cappi, M., et al. 2013, MNRAS, 431, 2441
Fabian, A. C., Kara, E., Walton, D. J., et al. 2013, MNRAS, 429, 2917
Fabian, A. C., Zoghbi, A., Ross, R. R., et al. 2009, Nature, 459, 540
Kara, E., Alston, W. N., Fabian, A. C., et al. 2016, MNRAS, 462, 511
Kara, E., Fabian, A. C., Cackett, E. M., Miniutti, G., & Uttley, P. 2013, MNRAS, 430, 1408
Kara, E., Fabian, A. C., Marinucci, A., et al. 2014, MNRAS, 445, 56
Kara, E., Zoghbi, A., Marinucci, A., et al. 2015, MNRAS, 446, 737
Kotov, O., Churazov, E., & Gilfanov, M. 2001, MNRAS, 327, 799
Laha, S., Dewangan, G. C., & Kembhavi, A. K. 2011, ApJ, 734, 75
Lyubarskii, Yu. E. 1997, MNRAS, 292, 679
Matt, G., Bianchi, S., Guainazzi, M., et al. 2011, A&A, 533, A1
Miniutti, G., & Fabian, A. C. 2004, MNRAS, 349, 1435
Nardini, E., Fabian, A. C., & Walton, D. J. 2012, MNRAS, 423, 3299
Nowak, M. A., Vaughan, B. A., Wilms, J., Dove, J. B., & Begelman, M. C. 1999, ApJ, 510, 874
Reis, R. C., Fabian, A. C., Reynolds, C. S., et al. 2012, ApJ, 745, 93
Silva, C. V., Uttley, P., & Costantini, E. 2016, A&A, 596, 79
Sriram, K., Agrawal, V. K., & Rao, A. R. 2009, ApJ, 700, 1042
Stella, L., & Angelini, L. 1992, in ASP Conf. Ser., Astronomical Data Analysis Software and Systems Vol. 25, W. M. Diana, B. Chris & B. Jeannette, 103
Tanaka, Y., Nandra, K., Fabian, A. C., et al. 1995, Natur, 375, 659
Veron-Cetty, M. P., & Veron, P. 2010, A&A, 518, 10
Zoghbi, A., Fabian, A. C., Uttley, P., et al. 2010, MNRAS, 401, 2419